Laser Preparation of Graphene-Based Photothermal De-icing Surface

WANG Qiang[1,2], *ZHANG Yecan*[1], *LIU Shaolong*[1], *LEI Fan*[2], *HAN Dongdong*[1,3*]

1. State Key Laboratory of Integrated Optoelectronics, College of Electronic Science and Engineering, Jilin University, Changchun 130012, P.R.China;
2. Institute of Chemical Materials, China Academy of Engineering Physics, Mianyang 621900, P.R.China;
3. Key Laboratory of Icing and Anti/De-icing, China Aerodynamics Research and Development Center, Mianyang 621000, P.R.China

(Received 10 March 2023; revised 15 June 2023; accepted 10 August 2023)

Abstract: Icing on significant equipment, such as airplane wings, wind turbines, and solar panels, causes aerodynamic changes and important component deformation, which seriously threatens operation safety. However, fabricating flexible, conformal, and robust photothermal de-icing surfaces remains challenging. Herein, a porous and hydrophobic laser induced graphene (LIG) based photothermal anti-frosting/de-icing surface is designed and fabricated by direct laser writing technologies. The LIG film is prepared by laser irradiation on polyimide (PI) film. After laser irradiation, the LIG film exhibits porous structures and a high C/O ratio. Due to the existence of porous structures and a high C/O ratio, the LIG film shows hydrophobic properties (CA, ~123.2°), high absorption, and good photothermal conversion. Thus, the LIG film displays photothermal anti-frosting and de-icing abilities. The work shows great potential in developing flexible, conformal, and robust photothermal anti-frosting/de-icing surfaces.

Key words: laser fabrication; graphene; photothermal conversion; anti-frosting; de-icing

CLC number: TN249 **Document code**: A **Article ID**: 1005-1120(2023)S1-0129-09

0 Introduction

Icing on significant equipment (such as airplane wings, wind turbines, and solar panels) usually causes aerodynamic changes and important component deformation, which seriously threatens equipment operation safety[1-5]. Currently, many important de-icing technologies are developed, including manual de-icing, mechanical de-icing, thermal de-icing, laser de-icing, electromagnetic de-icing and ultrasonic de-icing[6-11]. Among various de-icing technologies, manual de-icing is the most commonly used. However, manual de-icing suffers from low efficiency and high cost. In particular, it is very difficult to perform manual de-icing in dangerous environments. In recent years, researchers have begun to investigate new-concept de-icing technologies.

Inspired by lotus leaves, hydrophobic self-cleaning surfaces display great potential in anti-frosting and de-icing abilities[12-16]. The mechanism of the hydrophobic surface for anti-frosting and de-icing could be attributed to water droplets easily rolling away from the tilted hydrophobic surface under gravity[17-20]. Therefore, hydrophobic surfaces are able to reduce the hanging water before freezing, suppress or delay the formation of ice crystals, and reduce the adhesion between ice crystals and the contact interface[21-23]. Compared with traditional de-icing technologies, hydrophobic surfaces have the advantages of low energy consumption and environmental friendliness[24-26]. Usually, hydrophobic surfaces consist of low surface energy materials and own high roughness[27-31]. Hydrophobic surfaces can be prepared by coating hydrophobic materials on

*Corresponding author, E-mail address: handongdong@jlu.edu.cn.

How to cite this article: WANG Qiang, ZHANG Yecan, LIU Shaolong, et al. Laser preparation of graphene-based photothermal de-icing surface[J]. Transactions of Nanjing University of Aeronautics and Astronautics, 2023, 40(S1): 129-137.
http://dx.doi.org/10.16356/j.1005-1120.2023.S1.012

structured substrates. However, facing harsh working conditions, the microstructures and surface chemical properties of the coating may be destroyed, leading to reduction or even loss of hydrophobic ability.

Carbon materials can withstand high and low temperature alternation, solar radiation, acid rain and other harsh natural environments[32-36]. As a typical carbon material, graphene shows excellent physical properties, including flexibility, light weight, high conductivity, and high photothermal conversion ability[37-42]. Recently, various graphene-based electro-thermal de-icing surfaces have been designed and fabricated[43-45]. However, electro-thermal de-icing surfaces consume a large amount of electric energy. In particular, graphene owns wide spectrum absorption and good photothermal conversion efficiency[46-50], which raises the temperature in a short time. It is highly desired to develop a graphene-based photothermal de-icing surface.

In this work, a porous and hydrophobic laser-induced graphene (LIG)-based photothermal anti-frosting/de-icing surface is designed and fabricated by direct laser writing technologies. The LIG film shows hydrophobic properties, high absorption, and good photothermal conversion. Especially, the LIG film displays excellent photothermal anti-frosting and de-icing abilities.

1 Experimental Section

1.1 Preparation of LIG surface

As shown in Fig.1, LIG was prepared by direct laser writing on a PI film (Kapton, thickness 0.012 5 mm, DuPont, USA). The wavelength of the laser is 450 nm. The maximum power is 3 W. The spot size is 100 μm. First, the PI film was cleaned with ethanol and deionized water. After cleaning, the PI film was dried at room temperature. Next, the PI film was placed on the moving stage. The z-axis of the moving stage was adjusted to ensure that the laser was focused on the top surface of the PI film. Then, the desired pattern was uploaded to the laser processing control software.

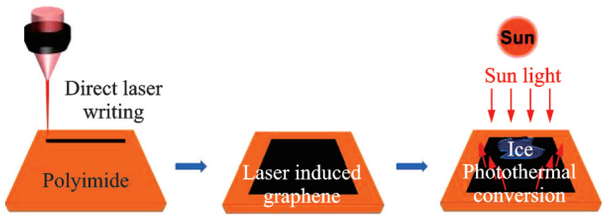

Fig.1 Schematic diagram of laser preparation of graphene-based photothermal de-icing surface

1.2 Characterization

X-ray photoelectron spectroscopy (XPS) was performed by an ESCALAB 250 spectrometer. Raman spectroscopy was obtained using a LabRAM HR Evolution. Confocal laser scanning microscopy (CLSM) images of the three-dimensional topography were obtained using a LEXT 3D measuring laser microscope (OLS4100, Japan). Scanning electron microscopy (SEM) images of the surface topography were obtained using a JEOL JSM-7500F field emission scanning electron microscope. The static water contact angle (CA) was measured by a contact angle system (SDC-350, SIN DIN Company, China). A deionized water droplet with a volume of 2 μL was gently dropped onto the sample surface with a pipette. A Shimadzu UV-3600 spectrophotometer (LISR-UV3100) was used to measure the reflectance, transparency, and absorbance in the wavelength range of 300—2 000 nm.

1.3 Photothermal performance characterization

A xenon lamp (CHF-XM500) was employed to simulate sunlight. A power meter is used to measure the intensity of simulated sunlight. The output power of the xenon lamp was adjusted by changing the distance between the xenon lamp and the sample surface. The light intensity on the surface of the LIG sample is 1 kW/m^2. A thermal imager (FOTRIC 286) was used to measure the temperature change of the sample surface under simulated sunlight.

1.4 Anti-frosting performance characterization

First, a 10 mm×10 mm LIG film was fixed on an aluminum block. The LIG film was kept tilted at 45°. Next, the aluminum block was placed on the re-

frigerated device at a temperature of −5 ℃. A humidifier was employed to simulate a high-humidity environment. A digital camera was used to record the frosting process on the LIG surface under light irradiation and without light irradiation. Then, the mass change of frost on the LIG surface was measured by a high-precision electronic mass balance under light irradiation and without light irradiation.

1.5 De-icing performance characterization

First, a 10 mm×10 mm LIG film was placed on the refrigerated devices. A water droplet(50 μL) was dropped on the surface of the LIG film. Next, the water droplet froze and became hemispherical ice. Then, the LIG film bearing ice was fixed on an aluminum block. The LIG film was kept tilted at 45°. Afterwards, the aluminum block was placed on the refrigerated device at a temperature of −5 ℃. A digital camera was used to record the photothermal de-icing performance of the LIG film under light irradiation and without light irradiation. In regard to the adhesion between ice and LIG film, the adhesion force was measured using a force gauge under light irradiation. The force gauge pushed the ice in the horizontal direction. The force was obtained by extraction from the thrust peak value.

2 Results and Discussion

2.1 Characterization of LIG surface

The color of PI is yellow. Whereas, the color of the laser-treated area is black (Fig.2(a)). The PI film and LIG film are both flexible, which can be used to integrated on targeted surfaces (Fig.2(b)). The color change after laser ablation indicates that carbonization occurs on the laser-treated area on the PI surface. The chemical composition changes can be examined by XPS. The XPS spectrum of the laser-treated area is shown in Fig.3. The C/O ratio is ~8.56. For the PI film, the C/O ratio is ~3.2[51]. Compared with PI, the increasing C/O ratio indicates that efficient carbonization occurs in the laser-treated area. It is worth mentioning that the increase in the carbon element ratio contributes to the preparation of a much more hydrophobic surface.

(a) Flexibility of LIG

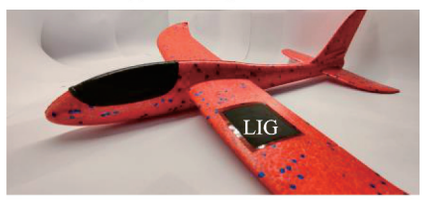

(b) Integration of LIG

Fig.2 Photographs of LIG

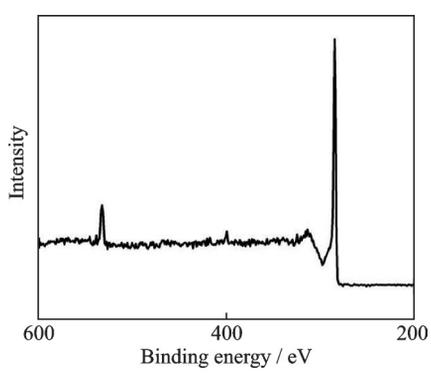

Fig.3 XPS spectrum of LIG

To confirm whether there is graphene in the carbonized region, a Raman test was conducted on the laser-treated area. As shown in Fig.4, there is no typical peak for the PI surface. The laser focus spot shows high temperatures (~1 000 ℃). The high temperatures will contribute to PI pyrolysis upon laser irradiation. Whereas, there are three typical peaks for the laser-treated area. Three typical peaks are located at 1 350, 1 582 and 2 700 cm^{-1}, corresponding to the *D* peak, *G* peak, and 2*D* peak, respectively. The ratio of I_D/I_G is ~0.43, indicating

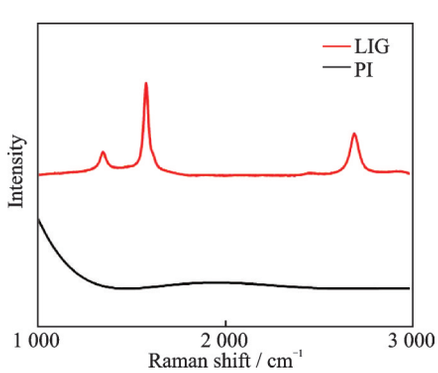

Fig.4 Raman spectra of PI and LIG

that the laser-treated area is highly graphitized after laser irradiation. The existing 2*D* peak demonstrates graphene formation after laser ablation.

The main reasons for the hydrophobic surface are the low surface energy (such as high carbon content) and high roughness (such as hierarchical micro/nanostructures). To observe the surface topography of LIG, we carried out CLSM. As shown in Fig.5, there is a linear groove structure on the LIG surface. The formation of a linear groove structure is due to the linear laser scanning treatment. The cross-section height curve of LIG is shown in Fig.6. The period of the groove structure is ~100 μm. The height of the groove structure is ~14 μm. The Ra of LIG is ~1.9 μm. The undulation of the cross-section height curve indicates that there are hierarchical micro/nanostructures on the surface of the linear groove structure. Hierarchical micro/nanostructures are beneficial for improving surface roughness.

To further explore the nanostructures on the LIG surface, SEM was carried out. Fig.7 is the high magnification SEM image of LIG. There are nano porous structures and nano debris on the LIG surface. As we mentioned above, the laser focus spot shows high temperature(~1 000 ℃). The high temperature will contribute to PI melting, vaporization, and pyrolysis upon laser irradiation. Therefore, porous structures formed because PI pyrolysis occurred in the form of gas under laser irradiation. Gas escape caused porous structure formation.

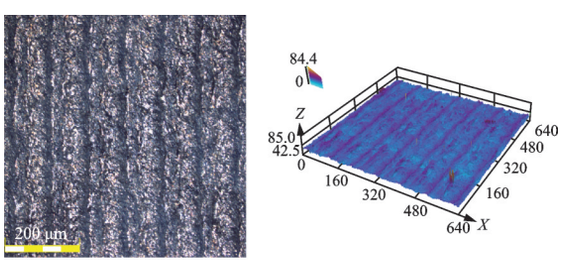

(a) 2D image (b) 3D CLSM image

Fig.5 CLSM images of LIG

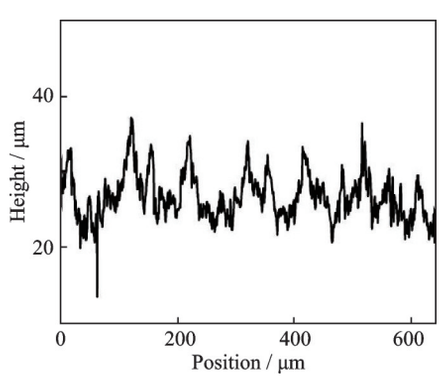

Fig.6 Cross-section height curve of LIG

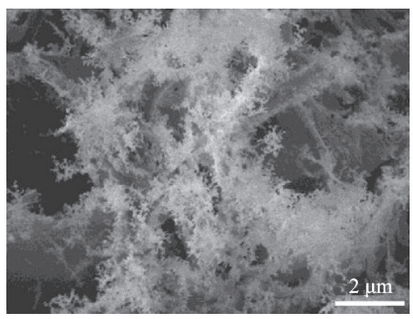

Fig.7 High magnification SEM image of LIG

The LIG surface has a high carbon content and hierarchical micro/nanostructures, which may lead to hydrophobicity. Furthermore, the water CAs of PI and LIG were measured to investigate the surface wettability. As shown in Fig.8, the water CA of PI is ~86.3°. The water CA of LIG is ~123.2°. Compared with PI, the higher water CA of LIG is due to its higher C/O ratio and hierarchical micro/nanostructures. The hydrophobicity of LIG has great potential in anti-frosting and anti-icing applications.

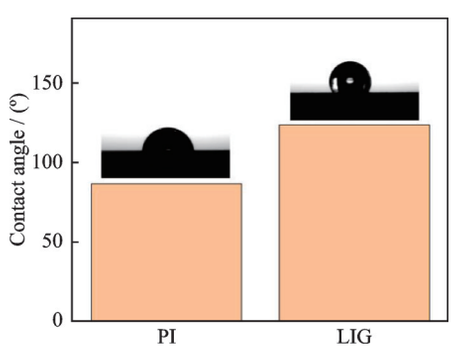

Fig.8 Water contact angle images of PI and LIG

2.2 Photothermal performance of LIG

Material reflectance, transparency, and absorption play important roles in photothermal conversion. To investigate the photothermal performance of LIG, we first measured the reflectance, transparency, and absorption of LIG. As shown in Fig.9, the reflectance of LIG at 500, 1 000 and 1 500 nm are

~6.6%, ~8.6%, and ~10%, respectively, and the transparencies of LIG at 500, 1 000 and 1 500 nm are ~0%, ~0%, and ~0%, respectively. Therefore, the absorption of LIG at 500, 1 000 and 1 500 nm are calculated to be ~93.4%, ~91.4%, and ~90%, respectively (Fig. 9). LIG shows a high absorption (⩾90%) in both the visible and near-infrared bands. The high absorption may be attributed to the microporous structure on the LIG surface trapping light, which significantly improves absorption.

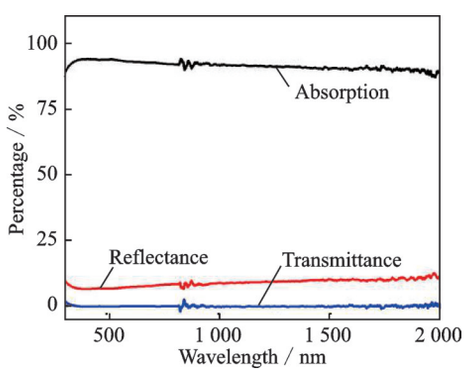

Fig.9 Reflectance, transparency spectrum, and absorbance spectrum of LIG

High absorption is beneficial for photothermal conversion ability. To examine the photothermal conversion ability of the PI surface and LIG surface, the temperature rising curves of PI and LIG along with light irradiation time under 1 kW/m^2 were measured (Fig.10). As shown in Fig.10, the PI surface temperature increased from 17.1 ℃ to 35.1 ℃ after 500 s of light irradiation. In regard to LIG, the LIG surface temperature increased from 17.1 ℃ to 40.7 ℃ after 500 s of light irradiation, which is 5.6 ℃ higher than the PI surface temperature. The higher surface temperature of LIG may be because the absorption of LIG is higher than that of PI. A high surface temperature indicates that LIG can be used as an anti-frosting and de-icing surface. In addition, it is worth noting that the slope of the temperature rise curve of LIG is higher than the slope of the temperature rise curve of PI, indicating that the temperature rise rate of LIG is higher than that of PI. The higher temperature rise rate contributes to a shorter ice melting time.

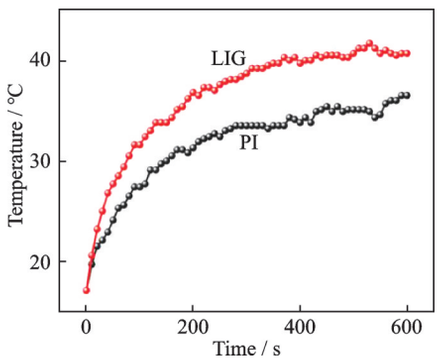

Fig.10 Surface temperature variations of the PI and LIG surfaces

2.3 Anti-frosting performance of LIG

LIG has good photothermal conversion ability and can be used as an anti-frosting surface. As shown in Fig.11(a), LIG frosted in a humid environment when the surrounding temperature was below 0 ℃. Initially, small water droplets deposit on the LIG surface. After 2 min, the deposited small droplets become frost on the LIG surface. Obvious frost can be observed on the LIG surface. After 4 min, the surface was completely frosted. In regard to the LIG surface with light irradiation, there is almost no frost at the same time (Fig.11(b)). The reason for anti-frosting is due to the photothermal conversion ability of LIG. The surface temperature of LIG increased under light irradiation, which prevented the frosting process of small water droplets.

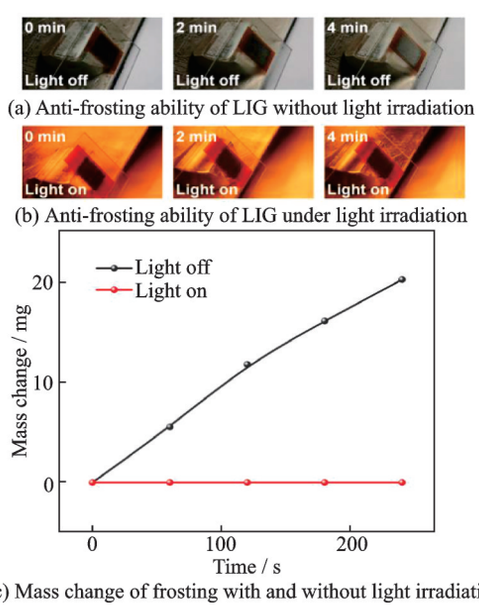

(a) Anti-frosting ability of LIG without light irradiation

(b) Anti-frosting ability of LIG under light irradiation

(c) Mass change of frosting with and without light irradiation

Fig.11 Anti-frosting ability of LIG

To quantitatively evaluate the anti-frosting performance of LIG, the curve of the frost deposited mass change on the LIG surface over time was measured under light irradiation and without light irradiation (Fig.11(c)). The frosting mass on the surface of the LIG surface increased with exposure time without light irradiation. The maximum mass change within 240 s is ~6.2 mg. Whereas, there was no frosting on the LIG surface, and the mass hardly changed for LIG under light irradiation, demonstrating the anti-frosting ability of LIG.

2.4 De-icing performance of LIG

In addition to photothermal anti-frosting ability, LIG also shows photothermal de-icing ability. As shown in Fig.12(a), the ice did not slide on the tilted LIG surface. Whereas, the ice began to melt at 43 s under light irradiation (Fig.12(b)). The ice began to slide at ~60 s. The ice melted and slid away from the LIG surface at ~120 s. This phenomenon can be explained as follows: (1) The LIG surface temperature increased with increasing light irradiation time. (2) The LIG heated the adhesion ice, and the ice began to melt. (3) The adhesion between ice and LIG decreased, and ice slid away because of the hydrophobicity of the LIG surface.

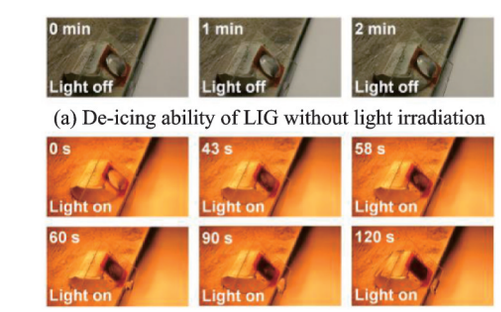

(a) De-icing ability of LIG without light irradiation

(b) De-icing ability of LIG under light irradiation

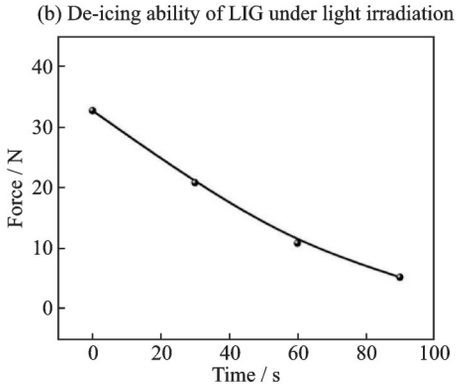

(c) Adhesion force between ice and LIG under light irradiation

Fig.12 De-icing ability of LIG

To quantitatively demonstrate the abovementioned reasons, the adhesion between ice and LIG was measured. As shown in Fig.12(c), the adhesion between ice and LIG decreased from 32.66 N to 5.12 N. The heat of the LIG surface generated by light irradiation effectively melted the interface between the ice and LIG, reducing the adhesion between the ice and LIG. The decreased adhesion leads to ice sliding away from the LIG surface.

3 Conclusions

Direct laser writing technologies were employed to fabricate a porous and hydrophobic LIG-based photothermal anti-frosting/de-icing surface. The resulted LIG film shows high absorption and good photothermal conversion. Due to the high absorption and good photothermal conversion, the LIG film exhibits photothermal anti-frosting and de-icing abilities with high performances. This work shows great potential in developing flexible and photothermal anti-frosting/de-icing surfaces.

References

[1] YI X, CHEN K, WANG K, et al. Application of CFD technology in wind turbine icing prober design[J]. Transactions of Nanjing University of Aeronautics & Astronautics, 2013, 30(3): 264-269.

[2] DHYANI A, CHOI W, GOLOVIN K, et al. Surface design strategies for mitigating ice and snow accretion[J]. Matter, 2022, 5(5): 1423-1454.

[3] BAO X, ZHOU Z, WANG Y. Review: Distributed time-domain sensors based on Brillouin scattering and FWM enhanced SBS for temperature, strain and acoustic wave detection[J]. PhotoniX, 2021, 2(1): 14.

[4] KREDER M J, ALVARENGA J, KIM P, et al. Design of anti-icing surfaces: Smooth, textured or slippery?[J]. Nature Reviews Materials, 2016, 1(1): 1-15.

[5] WANG F, ZHUO Y, HE Z, et al. Dynamic anti-icing surfaces (DAIS)[J]. Advanced Science, 2021, 8(21): 2101163.

[6] WANG L, GONG Q H, ZHAN S H, et al. Robust anti-icing performance of a flexible superhydrophobic surface[J]. Advanced Materials, 2016, 28(35): 7729.

[7] PAN P, WU S P, XIAO Y, et al. A review on hydronic asphalt pavement for energy harvesting and

snow melting[J]. Renewable & Sustainable Energy Reviews, 2015, 48: 624-634.

[8] WEI K X, YANG Y, ZUO H Y, et al. A review on ice detection technology and ice elimination technology for wind turbine[J]. Wind Energy, 2020, 23(3): 433-457.

[9] HAN D D, CAI Q, CHEN Z D, et al. Bioinspired surfaces with switchable wettability[J]. Frontiers in Chemistry, 2020, 8: 692.

[10] KE J, SUN Y, DONG C, et al. Development of China's first space-borne aerosol-cloud high-spectral-resolution lidar: Retrieval algorithm and airborne demonstration[J]. PhotoniX, 2022, 3(1): 17.

[11] LIU Y, LI X, JIN J, et al. Anti-icing property of bio-inspired micro-structure superhydrophobic surfaces and heat transfer model[J]. Applied Surface Science, 2017, 400: 498-505.

[12] ZHU Y, WANG Z, LIU X, et al. Anti-icing/de-icing mechanism and application progress of bio-inspired surface for aircraft[J]. Transactions of Nanjing University of Aeronautics & Astronautics, 2022, 39(5): 541-560.

[13] FARHADI S, FARZANEH M, KULINICH S A. Anti-icing performance of superhydrophobic surfaces[J]. Applied Surface Science, 2011, 257(14): 6264-6269.

[14] WU B R, CUI X, JIANG H Y, et al. A superhydrophobic coating harvesting mechanical robustness, passive anti-icing and active de-icing performances[J]. Journal of Colloid and Interface Science, 2021, 590: 301-310.

[15] HAN D D, ZHANG Y L, CHEN Z D, et al. Carnivorous plants inspired shape-morphing slippery surfaces[J]. Opto-Electronic Advances, 2023, 6(1): 210163-1-210163-11.

[16] LIU X Q, ZHANG Y L, LI Q K, et al. Biomimetic sapphire windows enabled by inside-out femtosecond laser deep-scribing[J]. PhotoniX, 2022, 3(1): 1.

[17] BIEDERMANN F, NAU W M, SCHNEIDER H J. The hydrophobic effect revisited-studies with supramolecular complexes imply high-energy water as a noncovalent driving force[J]. Angewandte Chemie-International Edition, 2014, 53(42): 11158-11171.

[18] CHANDLER D. Interfaces and the driving force of hydrophobic assembly[J]. Nature, 2005, 437(7059): 640-647.

[19] JIANG H B, ZHANG Y L, HAN D D, et al. Bioinspired fabrication of superhydrophobic graphene films by two-beam laser interference[J]. Advanced Functional Materials, 2014, 24(29): 4595-4602.

[20] TANG B H, WANG Q, HAN X C, et al. Fabrication of anti-icing/de-icing surfaces by femtosecond laser[J]. Frontiers in Chemistry, 2022, 10: 1073473.

[21] DOTAN A, DODIUK H, LAFORTE C, et al. The relationship between water wetting and ice adhesion[J]. Journal of Adhesion Science and Technology, 2009, 23(15): 1907-1915.

[22] KENZHEBAYEVA A, BAKBOLAT B, SULTANOV F, et al. A mini-review on recent developments in anti-icing methods[J]. Polymers, 2021, 13(23): 4149.

[23] LIN Y, CHEN H, WANG G, et al. Recent progress in preparation and anti-icing applications of superhydrophobic coatings[J]. Coatings, 2018, 8(6): 208.

[24] DI M R, LABIANCA C, CARBONE G, et al. Recent advances in hydrophobic and icephobic surface treatments of concrete[J]. Coatings, 2020, 10(5): 449.

[25] KIM M H, KIM H, LEE K S, et al. Frosting characteristics on hydrophobic and superhydrophobic surfaces: A review[J]. Energy Conversion and Management, 2017, 138: 1-11.

[26] KOZBIAL A, ZHOU F, LI Z T, et al. Are graphitic surfaces hydrophobic?[J]. Accounts of Chemical Research, 2016, 49(12): 2765-2773.

[27] AN H J, LIU G M, CRAIG V S J. Wetting of nanophases: Nanobubbles, nanodroplets and micropancakes on hydrophobic surfaces[J]. Advances in Colloid and Interface Science, 2015, 222: 9-17.

[28] MUHR V, WILHELM S, HIRSCH T, et al. Upconversion nanoparticles: From hydrophobic to hydrophilic surfaces[J]. Accounts of Chemical Research, 2014, 47(12): 3481-3493.

[29] SAMYN P. Wetting and hydrophobic modification of cellulose surfaces for paper applications[J]. Journal of Materials Science, 2013, 48(19): 6455-6498.

[30] YI J, ZHOU H, WEI W H, et al. Micro-/nano-structures fabricated by laser technologies for optoelectronic devices[J]. Frontiers in Chemistry, 2021, 9: 823715.

[31] WANG H, ZHANG Y L, HAN D D, et al. Laser fabrication of modular superhydrophobic chips for reconfigurable assembly and self-propelled droplet manipulation[J]. PhotoniX, 2021, 2(1): 1-13.

[32] GONG Y T, XIE L, CHEN C H, et al. Bottom-up hydrothermal carbonization for the precise engineering of carbon materials[J]. Progress in Materials Science, 2023, 132: 101048.

[33] LYU C, BAI X, NING S, et al. Nanostructured materials for photothermal carbon dioxide hydrogenation: regulating solar utilization and catalytic perfor-

mance[J]. ACS Nano, 2023, 17(3): 1725-1738.
[34] ZHOU H, LI J C, HAN X C, et al. Deformable moisture-activated all-solid-state planar microsupercapacitors[J]. Applied Physics Letters, 2023, 122(10): 103901.
[35] LIU Y Q, MAO J W, CHEN Z D, et al. Three-dimensional micropatterning of graphene by femtosecond laser direct writing technology[J]. Optics Letters, 2020, 45(1): 113-116.
[36] LIU Y Q, CHEN Z D, MAO J W, et al. Laser fabrication of graphene-based electronic skin[J]. Frontiers in Chemistry, 2019, 7: 461.
[37] HAN X C, WANG Q, CHEN Z D, et al. Laser-reduced graphene oxide for a flexible liquid sliding sensing surface[J]. Optics Letters, 2023, 48(3): 839-842.
[38] JIAO Z Z, ZHOU H, HAN X C, et al. Photothermal responsive slippery surfaces based on laser-structured graphene@ PVDF composites[J]. Journal of Colloid and Interface Science, 2023, 629: 582-592.
[39] MAO J W, HAN D D, ZHOU H, et al. Bioinspired superhydrophobic swimming robots with embedded microfluidic networks and photothermal switch for controllable marangoni propulsion[J]. Advanced Functional Materials, 2023, 33(6): 2208677.
[40] HAN D D, CHEN Z D, LI J C, et al. Airflow enhanced solar evaporation based on Janus graphene membranes with stable interfacial floatability[J]. Acs Applied Materials & Interfaces, 2020, 12(22): 25435-25443.
[41] ZHANG Y L, MA J N, LIU S, et al. A "Yin"-"Yang" complementarity strategy for design and fabrication of dual-responsive bimorph actuators[J]. Nano Energy, 2020, 68: 104302.
[42] CHANG H, LIU Z, YANG S, et al. Graphene-driving strain engineering to enable strain-free epitaxy of AlN film for deep ultraviolet light-emitting diode[J]. Light: Science & Applications, 2022, 11(1): 88.
[43] ZHAO Z H, CHEN H W, LIU X L, et al. Development of high-efficient synthetic electric heating coating for anti-icing/de-icing[J]. Surface & Coatings Technology, 2018, 349: 340-346.
[44] ZHANG Y L, LI J C, ZHOU H, et al. Electro-responsive actuators based on graphene[J]. Innovation, 2021, 2(4): 100168.
[45] YOU R, LIU Y Q, HAO Y L, et al. Laser fabrication of graphene-based flexible electronics[J]. Advanced Materials, 2020, 32(15): 1901981.
[46] BASIRI A, RAFIQUE MZE, BAI J, et al. Ultrafast low-pump fluence all-optical modulation based on graphene-metal hybrid metasurfaces[J]. Light: Science & Applications, 2022, 11(1): 102.
[47] THEERTHAGIRI J, KARUPPASAMY K, LEE S J, et al. Fundamentals and comprehensive insights on pulsed laser synthesis of advanced materials for diverse photo- and electrocatalytic applications[J]. Light: Science & Applications, 2022, 11(1): 250.
[48] YI C H, PARK H C, PARK M J. Strong interlayer coupling and stable topological flat bands in twisted bilayer photonic Moiré superlattices[J]. Light: Science & Applications, 2022, 11(1): 289.
[49] IN C, KIM U J, CHOI H. Two-dimensional Dirac plasmon-polaritons in graphene, 3D topological insulator and hybrid systems[J]. Light: Science & Applications, 2022, 11(1): 313.
[50] LI R, DONG Y, QIAN F, et al. $CsPbBr_3$/graphene nanowall artificial optoelectronic synapses for controllable perceptual learning[J]. PhotoniX, 2023, 4(1): 4.
[51] LIN J, PENG Z, LIU Y, et al. Laser-induced porous graphene films from commercial polymers[J]. Nature Communications, 2014, 5(1): 5714.

Acknowledgements This work was supported in part by the Key Laboratory of Icing and Anti/De-icing of CARDC (No.IADL 20210404), the National Natural Science Foundation of China (NSFC)(No.62275100), and Jilin Province Development and Reform Commission Project (No. 2022C047-4).

Authors Mr. **WANG Qiang** received the B.S. degree in Electronic Information Engineering from Nanjing University of Science and Technology, Nanjing, China, in 2022. Currently, he is a master student at Jilin University, China. His research interest has been focused on laser preparation of graphene-based photothermal de-icing surface.

Dr. **HAN Dongdong** received his B.S. (2013) and Ph.D. (2018) from College of Electronic Science and Engineering, Jilin University, China. Currently, his research interest is focused on laser fabrication of graphene-based MEMS and de-icing surface.

Author contributions Mr. **WANG Qiang** contributed data components and wrote the manuscript. Mr. **ZHANG Yecan**, Mr. **LIU Shaolong**, and Mr. **LEI Fan** contributed data components. Dr. **HAN Dongdong** designed the study and wrote the manuscript. All authors commented on the manuscript draft and approved the submission.

Competing interests The authors declare no competing interests.

(Prodution Editor: SUN Jing)

石墨烯基光热除冰表面的激光制备

王 强[1,2]，张业灿[1]，刘少龙[1]，雷 凡[2]，韩冬冬[1,3]

（1.吉林大学电子科学与工程学院集成光电子学国家重点实验室，长春 130012，中国；
2.中国工程物理研究院化工材料研究所，绵阳 621900，中国；
3.中国空气动力研究与发展中心结冰与防除冰重点实验室，绵阳 621000，中国）

摘要：重要设备，如飞机机翼、风力涡轮机、太阳能电池板等结冰会引起空气动力学形状变化和重要部件变形，严重威胁运行安全。然而，制造柔性、共形的光热除冰表面仍然具有挑战性。本文采用激光直写技术，设计并制备了多孔疏水的激光诱导石墨烯（Laser induced grapheme，LIG）基光热抗霜除冰表面。采用激光照射聚酰亚胺（Polyimide，PI）薄膜制备LIG薄膜。激光照射后，LIG薄膜呈现多孔结构和高C/O比。由于多孔结构和高C/O比的存在，LIG膜具有疏水性（CA，～123.2°）、高吸收率和良好的光热转化率，因此，LIG薄膜具有光热抗霜除冰能力。本文工作显示了开发柔性、共形的光热抗霜/除冰表面的巨大潜力。

关键词：激光加工；石墨烯；光热转换；抗霜；除冰